Atmos. Chem. Phys. Discuss., 9, 13801–13842, 2009
www.atmos-chem-phys-discuss.net/9/13801/2009/

Atmospheric Chemistry and Physics Discussions

This discussion paper is/has been under review for the journal *Atmospheric Chemistry and Physics (ACP)*. Please refer to the corresponding final paper in *ACP* if available.

Evidence of ice crystals at cloud top of Arctic boundary-layer mixed-phase clouds derived from airborne remote sensing

A. Ehrlich[1,*], M. Wendisch[1,*], E. Bierwirth[2], J.-F. Gayet[3], G. Mioche[3], A. Lampert[4], and B. Mayer[5]

[1]Johannes Gutenberg-University Mainz, Institute for Atmospheric Physics, Mainz, Germany
[2]Lab. for Atmospheric and Space Physics (LASP), University of Colorado, Boulder, USA
[3]Lab. de Météorologie Physique (LAMP), Université Blaise Pascal, Aubière Cedex, France

[4]Alfred Wegener Institute for Polar and Marine Research (AWI), Potsdam, Germany
[5]Inst. of Atmospheric Physics, German Aerospace Center (DLR), Oberpfaffenhofen, Germany
[*]now at: Leipzig Institute for Meteorology (LIM), University of Leipzig, Leipzig, Germany

Received: 10 June 2009 – Accepted: 15 June 2009 – Published: 23 June 2009

Correspondence to: A. Ehrlich (a.ehrlich@uni-leipzig.de)

Published by Copernicus Publications on behalf of the European Geosciences Union.

Abstract

The vertical distribution of ice crystals in Arctic boundary-layer mixed-phase (ABM) clouds was investigated by airborne remote sensing and in situ measurements during the Arctic Study of Tropospheric Aerosol, Clouds and Radiation (ASTAR) campaign in March and April 2007. From airborne measurements of spectral solar radiation reflected by the ABM clouds information on the spectral absorption of solar radiation by ice and liquid water cloud particles is derived. It is shown by calculation of the vertical weighting function of the measurements that the observed absorption of solar radiation is dominated by the upper cloud layers (50% within 200 m from cloud top). This vertical weighting function is shifted even closer to cloud top for wavelengths where absorption by ice is dominating. On this basis an indicator of the vertical distribution of ice crystals in ABM clouds is designed.

Applying the in situ measured microphysical properties, the cloud top reflectance was calculated by radiative transfer simulations and compared to measurements. It is found that ice crystals near cloud top (mixed-phase cloud top layer) are necessary to reproduce the measurements at wavelengths where absorption by ice is dominating. The observation of backscatter glories on top of the ABM clouds generally indicating liquid water droplets does not contradict the postulated presence of ice crystals. Radiative transfer simulations reproduce the observed glories even if the cloud top layer is of mixed-phase character.

1 Introduction

Due to the low temperatures Arctic boundary-layer mixed-phase (ABM) clouds consisting of both supercooled liquid water droplets and solid ice crystals simultaneously are common. Such ABM clouds have been observed and investigated during numerous Arctic field experiments (Cober et al., 2001; Turner et al., 2003; Korolev et al., 2003; Boudala et al., 2004; McFarquhar and Cober, 2004; Shupe et al., 2008). As Shupe and

ACPD

9, 13801–13842, 2009

Intrieri (2004) have shown, ABM clouds are the most important contributors to the Arctic surface radiation budget. Their radiative impact is highly variable and depends on surface albedo, aerosol particle concentration, cloud water content, cloud particle size and thermodynamic phase, (Curry et al., 1996; Shupe and Intrieri, 2004; Ehrlich et al., 2008b). Therefore, an understanding of the physical processes controlling the nucleation and spatial distribution of ice crystals and liquid water droplets in ABM clouds is needed.

A simplified scheme of ABM clouds is presented by Harrington et al. (1999) in which the coexistence of ice and liquid water relies on the balance between the nucleation rate of liquid water droplets and ice crystals, the ice crystal growth rate, and the removal of ice nuclei by precipitating ice crystals. The persistence of updrafts responsible for the formation of liquid water droplets by condensation is ensured by radiative cooling at the cloud top and the heat release of the open sea. In this scheme liquid water droplet nucleation is most efficient within the updrafts at cloud top and exceeds the ice crystal nucleation rate. This process leads to the typical vertical structure of ABM clouds with a cloud top layer dominated by liquid water and an ice layer with precipitating ice crystals below (e.g., Pinto, 1998; Shupe et al., 2006; McFarquhar et al., 2007).

This simplified scheme is altered by a number of factors which need to be maintained in equilibrium to assure the persistence of the ABM clouds. Only slight changes (e.g. increase of ice crystal nucleation rate or decrease of ice crystal sedimentation rate) may result in a complete glaciation of the ABM cloud as shown by Harrington et al. (1999). A glaciation will shorten the life time and alter the radiative properties of ABM clouds significantly. In this regard ice crystal properties and ice nuclei play a crucial role by controlling the ice crystal concentration. However, the nucleation, growth and sedimentation of ice crystals are still not well understood which leads to discrepancies between observed and simulated ice crystal number concentrations (e.g., Morrison et al., 2008; Fan et al., 2008). As a consequence the results of cloud resolving dynamical models are highly sensitive to the parameterizations of these processes as shown by, e.g., Harrington et al. (1999); Morrison et al. (2005); Prenni et al. (2007). Morrison et al. (2005)

ACPD
9, 13801–13842, 2009

analyzed the importance of different ice production processes while Harrington et al. (1999) investigated the dependence of the life time of ABM clouds on temperature, ice crystal number concentration and ice crystal shape and found that the concentration of ice nuclei is the most determining parameter. An increase of the ice nuclei concentration results in a rapid glaciation of ABM clouds and reduces their life times. The concentration of cloud condensation nuclei which typically ranges magnitudes above the ice nuclei concentration has a minor impact.

These uncertainties in the simulations of ABM clouds suggest that information on the ice crystal properties is needed. Especially the vertical distribution of ice crystals will help to identify ice nucleation processes that are associated with distinct cloud layers (e.g. evaporation freezing at cloud top and cloud base). In situ measurements of ice crystal microphysical properties such as ice crystal size, number concentration and shape have been conducted for many years. For example, parameterizations of the ice volume fraction (ratio of ice to total water content) as a function of cloud temperature have been obtained from in situ measurements by Boudala et al. (2004); Korolev et al. (2003). However, due to the limitations in time and space in situ measurements can only give a snapshot of the complexity of Arctic clouds (Lawson et al., 2001; Cober et al., 2001; McFarquhar et al., 2007; Gayet et al., 2009). To globally and continuously derive information on the ice crystal properties remote sensing technologies on board of satellites or long-range aircrafts have to be applied.

The relative contribution of individual cloud layers to the overall retrieval of cloud properties from remote sensing was investigated by Platnick (2000). He found for vertically inhomogeneous liquid water clouds that the vertical weighting function (VWF) for the cloud top reflectance measurements has a maximum at the cloud top layer with an optical thickness less than 2. The calculated VWFs strongly depend on the solar zenith angle and the wavelength applied for the retrieval (1600 nm, 2200 nm or 3700 nm). The larger the wavelength and the solar zenith angle, the larger is the maximum of the VWF and the closer this maximum is located to the cloud top. These spectral differences in the VWFs at four different spectral bands of the Moderate Resolution Imaging Spectro-

radiometer (MODIS) were utilized by Chang and Li (2002, 2003) and recently by Chen et al. (2008) to estimate the vertical variation of the cloud droplet effective diameter from remote sensing for liquid water clouds.

In this study we present a similar method to characterize the vertical distribution of ice crystals in ABM clouds. Airborne measurements of spectral solar cloud reflectance and in situ data of cloud microphysical properties were utilized in combination with radiative transfer simulations. The measurements were performed during the Arctic Study of Tropospheric Aerosol, Clouds and Radiation (ASTAR) 2007 campaign in the vicinity of Svalbard (78° N, 15° E).

The instrumentation of the aircraft and the observations of spectral cloud top reflectance and microphysical properties are described in Sects. 2 and 3. The radiative transfer simulations combining in situ and remote sensing measurements are discussed in Sect. 4. Subsequently, the vertical weighting function of the remote sensing measurements and the inferred evidence of ice crystals at cloud top are investigated in Sects. 5 and 6. Finally, the visual observation of backscatter glories above ABM clouds is discussed in Sect. 7.

2 Instrumentation

During ASTAR 2007 the Polar 2 aircraft, owned by the Alfred Wegener Institute for Polar and Marine Research (AWI), Bremerhaven, Germany was equipped to probe ABM clouds with airborne remote sensing and in situ instruments. The Airborne Mobile Aerosol Lidar (AMALi) and the in situ instruments such as the Polar Nephelometer, Cloud Particle Imager (CPI), and Particle Measuring System (PMS) Forward Scattering Spectrometer Probe (FSSP-100) have been described in detail by Lampert et al. (2009) and Gayet et al. (2009), respectively. The study presented here analyzes data from the Spectral Modular Airborne Radiation measurement sysTem (SMART-Albedometer, Wendisch et al., 2001; Bierwirth et al., 2009). The specific configuration of the SMART-Albedometer operated during ASTAR 2007 has been introduced in detail by Ehrlich

ACPD
9, 13801–13842, 2009

et al. (2008a). It provides measurements of downwelling and upwelling spectral irradiances ($F_\lambda^\downarrow$, $F_\lambda^\uparrow$) simultaneously with upwelling nadir spectral radiance ($I_\lambda^\uparrow$). These data were used to calculated spectral cloud top reflectances R in the wavelength range between 350 nm and 2150 nm by

$$R(\lambda) = \frac{\pi\,\mathrm{sr} \cdot I_\lambda^\uparrow}{F_\lambda^\downarrow}. \quad (1)$$

In this definition $F_\lambda^\downarrow$ includes diffuse and direct solar radiation and is measured with respect to a horizontal plane $F_\lambda^\downarrow = F_\lambda^\downarrow(\cos\theta)$ with θ being the solar zenith angle. The spectral resolution of $R(\lambda)$ (full width at half maximum, FWHM) amounts to 2–3 nm in the wavelength range 350–950 nm and 9–16 nm for λ=950–2150 nm wavelength.

3 Measurements

ABM clouds have been observed during ASTAR-2007 (Ehrlich et al., 2008a; Gayet et al., 2009) in the area of the Greenland Sea. Cold air outbreaks with northerly winds initiated extended boundary-layer cloud fields. The convection above the relatively warm open sea allowed the coexistence of ice and liquid water in these clouds.

We focus on measurements conducted on 7 April 2007. The data collected on this day have already been analyzed with regard to their thermodynamic phase in Ehrlich et al. (2008a). During that day mixed-phase clouds were found to be dominant as revealed from both in situ measurements and the SMART-Albedometer.

3.1 In situ measurements

In situ measurements of microphysical and optical properties for the observed ABM clouds have been presented by Ehrlich et al. (2008a). Mixed-phase clouds with similar

ACPD
9, 13801–13842, 2009

properties observed during ASTAR 2007 on 9 April are investigated in detail by Gayet et al. (2009).

The vertical profiles of particle number concentrations, ice and liquid water content (IWC, LWC) and volumetric asymmetry parameter $\langle g \rangle$ obtained on 7 April 2007 is given in Fig. 1 (partly identical to Fig. 2 in Ehrlich et al., 2008a). Similar to the observations by Gayet et al. (2009) on 9 April 2007, it was found that the cloud top layer (1600–1200 m altitude) was dominated by liquid water droplets. This is indicated by the Polar Nephelometer measuring high asymmetry parameter ($\langle g \rangle$=0.83–0.86) which are typical for spherical liquid water droplets. The microphysical and optical properties of the liquid water droplets are summarized in Table 1. In total liquid water droplets have been observed between 800–1600 m with average IWC of 44 mg l^{-1} (maximum up to 240 mg l^{-1}) and droplet effective diameter of 15 μm. This corresponds to a liquid water path LWP of 35 g m^{-2} ($LWP = LWC \cdot \Delta z$). The fractional liquid water optical thickness τ_W was calculated from the volumetric extinction coefficient b_{ext} obtained from the in situ data ($\tau = b_{ext} \cdot \Delta z$) and amounts to τ_W=7.5.

The lower cloud part (1200–800 m altitude) contained a significant amount of ice crystals with IWC of 43 mg l^{-1} (maximum up to 200 mg l^{-1}). The ice water path IWP, fractional ice optical thickness τ_I and ice crystal effective diameter D^I_{eff} amount to IWP=17 g m^{-2}, τ_I=0.5 and D^I_{eff}=103 μm.

Ice crystals and liquid water droplets together result in a total cloud optical thickness $\tau = \tau_W + \tau_I$=8 and a total water path TWP of 52 g m^{-2}. The ice volume fraction $f_I = IWP/TWP$ and the ice optical fraction $f^*_I = \tau_I/\tau$ amounts to 0.33 and 0.06, respectively.

Below 800 m altitude precipitating ice crystals have been observed down to the surface by CPI and visual on board observations.

ACPD
9, 13801–13842, 2009

3.2 Cloud top reflectance measurements

The spectral cloud top reflectance measured above the ABM cloud is shown in Fig. 2a with its measurement uncertainty indicated by the gray area. These data have already been presented by Ehrlich et al. (2008a, Fig. 3). Below 1300 nm wavelength R is almost independent of wavelength except for the water vapor (λ=920 nm and λ=1130 nm) and oxygen absorption bands (λ=750 nm). At longer wavelengths the water vapor absorption is stronger (1350–1500 nm and 1800–1950 nm) which significantly increases the measurement uncertainties in these spectral ranges. Additionally, absorption due to the cloud particles (hereinafter called liquid water and ice absorption) is superimposed in the spectral range above 1300 nm wavelength. This is indicated by the imaginary part of the refractive indices $\tilde{n}_{\mathrm{i}}$ of liquid water and ice in Fig. 2b. For the measured R the local minima at λ=1490 nm and λ=1950 nm coincide with the maximum of $\tilde{n}_{\mathrm{i}}$ (maximum absorption by cloud particles). These data have been analyzed by Ehrlich et al. (2008a) to identify the cloud thermodynamic phase with two different ice indices.

Ehrlich et al. (2008a) stated that these ice indices are most sensitive to the upper cloud layers. Considering the observed vertical structure of the ABM cloud with liquid water dominating the cloud top, the ice indices derived for ABM clouds range slightly above values expected for clouds with liquid cloud top layer.

Therefore, we have applied the measured microphysical and radiative cloud properties in spectral radiative transfer simulations with the focus on the vertical structure of ABM clouds.

4 Simulated cloud top reflectance

The spectral solar radiative transfer simulations are performed with the libRadtran (Library for Radiative transfer) code by Mayer and Kylling (2005) for the wavelength range from 300 nm to 2200 nm adapted to the spectral resolution of the SMART-Albedometer.

ACPD
9, 13801–13842, 2009

For the one-dimensional (1-D) simulations the discrete ordinate solver DISORT version 2.0 by Stamnes et al. (1988) is applied. The meteorological input is similar to radiative transfer simulations presented by Ehrlich et al. (2008a). Profiles of static air temperature, relative humidity and static air pressure are obtained from a radio sounding at Ny-Ålesund/Svalbard (7 April 2007, 11:00 UTC). Corresponding to the observed marine clouds, the spectral surface albedo is represented by measurements above sea water obtained on 7 April (Ehrlich, 2009).

The spectral cloud optical properties (extinction coefficient, single scattering albedo and scattering phase function) have been calculated from optical properties of the individual cloud particles. Mie theory is applied for liquid water droplets. For the ice particles column-shaped ice crystals have been assumed. The optical properties of columns are provided by Yang and Liou (1996). For the simulations presented here the choice of the particle shape is of less importance. With regard to the wavelength range where ice absorption occurs, the predetermined effective diameter of the cloud particles characterizes the absorption independent of the particle shape. For the reflectance at visible wavelengths where absorption by cloud particles is negligible the scattering phase function of the ice crystals characterizes the scattering processes. However, the part of the scattering phase function relevant for the solar zenith angle used in the simulation (θ_0=71°) is similar for different ice crystal shapes.

4.1 Cloud optical thickness

Based on the in situ measurements the cloud was divided into two vertical sublayers representing the observed vertical structure of the ABM clouds. The cloud top layer (1200–1600 m) contains only liquid water droplets, whereas the cloud base (800–1200 m) contains both liquid water droplets and ice crystals. In Fig. 3 the cloud model used for the radiative transfer simulations is illustrated (Case A0). The microphysical and optical properties of each layer are given in Table 1.

ACPD
9, 13801–13842, 2009

4.1.1 Unscaled

The cloud top reflectance R simulated with the measured cloud optical properties (Case A0) is compared in Fig. 4a to R measured by the SMART-Albedometer (dashed black and green solid lines). The measurement uncertainty of R is indicated by the gray area. Especially for wavelengths shorter than 1800 nm the simulations (dashed line) range below the measured R and are outside the measurement uncertainties. This indicates that the cloud optical thickness is underestimated by the in situ measurements.

Beside the uncertainties of the in situ instruments, cloud inhomogeneities cause problems for deriving representative cloud optical properties. During the in situ probing several areas with low particle concentrations and low extinction coefficients b_{ext} were sampled related to the undulating structure of the ABM clouds. By averaging the measurements over the total time when the Polar Nephelometer measured considerable amounts of cloud particles (b_{ext}>0.05 km^{-1}) the mean values of b_{ext} underestimate the total cloud optical thickness. Maximum values of b_{ext}=35 km^{-1} and b_{ext}=20 km^{-1} have been measured for the liquid water droplets by the FSSP and Polar Nephelometer, respectively. In the thin ice layer the extinction coefficient of the ice crystal population amounts up to b_{ext}=13 km^{-1} as measured by the CPI. The underestimation of the cloud optical thickness due to cloud inhomogeneities can be reduced by an extended sampling time of the cloud. During ASTAR 2007 the ABM clouds have been probed during descents and ascents of the POLAR 2 with climbing rates of 200 m min^{-1} which reduces the sampling time for the individual vertical cloud layers even more.

4.1.2 Scaled

In order to adjust the results of the radiative transfer simulations to the measured R in the wavelength range λ<1800 nm the cloud optical thickness is scaled in the following simulations. Therefore, the total liquid water droplet and ice crystals concentration are varied. The scaling was applied by keeping cloud particle effective diameter, f_l^* and f_l unchanged. The microphysical and optical properties of the scaled cloud (hereafter

ACPD
9, 13801–13842, 2009

referred as Case A) are given in Table 1. With τ=18 the scaled total cloud optical thickness is more than doubled compared to the values derived from the in situ measurements.

The results of the radiative transfer simulations for Case A are shown in Fig. 4a as solid black line. For wavelengths less than 1400 nm the simulated R ranges within the uncertainties of the SMART-Albedometer measurements. However, at wavelengths where ice absorption is strong, as indicated by the imaginary refractive index displayed in Fig. 4b, the simulated R is higher than measured. This reveals that in the model cloud less ice crystals are present than indicated by the remote sensing measurements.

As shown by Ehrlich et al. (2008a) the spectral slope ice index I_S and the principle component analysis ice index I_P obtained for this particular ABM cloud are I_S=30 and I_P=2.3, respectively. From the simulated cloud top reflectance (Case A) values of I_S=13.4 and I_P=0.7 were calculated. These values are in the range which is derived for pure liquid water clouds, which is not surprising as the ice optical fraction f_I^*=0.06 of the simulated cloud is close to zero. The uncertainties of the measured f_I^* deduced from the simultaneous FSSP and CPI measurements are addressed in the following section.

4.2 Ice optical fraction

Based on the measured and scaled cloud optical properties of Case A the ice optical fraction f_I^* was varied between values corresponding to pure liquid water clouds (f_I^*=0.0) and a pure ice cloud (f_I^*=1.0). The microphysical and optical properties of the six simulated clouds with different ice optical fraction referred as Case B1–B6 are given in Table 2. The cloud geometry and the particle effective diameter $D_{\mathrm{eff}}^{\mathrm{w}}$, $D_{\mathrm{eff}}^{\mathrm{I}}$ are identical to the cloud Case A. Due to the differences in the scattering phase function of liquid water droplets and ice crystals, the cloud top reflectance increases with increasing f_I^* if the total cloud optical thickness is kept constant. In order to fit R in the wavelength range λ<1300 nm to the measured values, the total cloud optical thickness of Case B1–B6 was scaled for each cloud separately.

ACPD
9, 13801–13842, 2009

The results of the radiative transfer simulations are given in Fig. 5a. All simulations range between the two extreme cases; the pure liquid water cloud (B1, blue line) and the pure ice cloud (B6, red line). The corresponding ice indices I_S and I_P calculated from the simulations are listed in Table 3. The comparison with the measured ice indices indicates that the simulated cloud Case B5 with f_I^*=0.6 fits best to the measurements.

However, in Fig. 5a the analysis of the spectral structure of R in the wavelength range dominated by ice and liquid water absorption between 1400 nm and 2150 nm reveals that none of the simulated cases matches the measurements throughout the entire wavelength range. For low ice optical fractions f_I^*<0.4 the ice crystal concentration is too low and the resulting ice absorption too weak to reproduce the observed ice absorption minima. These minima were present in the measurements of the SMART-Albedometer at 1490 nm and 2000 nm wavelengths which agrees with the maxima in the refraction indices of ice plotted in Fig. 5b. However, at wavelengths where ice absorption is weaker (1600–1800 nm) R is in the range of the measurement uncertainties of the measured R for f_I^*<0.4. The opposite is obtained for the simulations with $f_I^*\geq$0.4. For these cases the ice absorption is strong enough to reproduce the spectral measurements at the ice absorption minima. However, the increasing ice absorption additionally reduces the cloud top reflectance at wavelengths between 1600 nm and 1800 nm. In this wavelength range the simulations with $f_I^*\geq$0.4 fail to fit the measured R.

It seems that there has to be another parameter which alters the spectral slope in the wavelength range dominated by ice and liquid water absorption (1400–2200 nm). From additional radiative transfer simulations using modified cloud models (not shown here) it was found that neither the particle effective diameter of the ice crystals and liquid water droplets nor the ice crystal shape are responsible for the observed spectral pattern of R. Therefore, in the following section the vertical weighting function (VWF) of the cloud top reflectance measurement is investigated.

ACPD
9, 13801–13842, 2009

5 VWF of reflectance measurements

We applied the methods described by Platnick (2000) to characterize the vertical weighting of the reflectance measurements in the wavelength range dominated by ice and liquid water absorption (1300–1800 nm).

Platnick (2000) proposed to use the maximum vertical photon penetration as VWF of R. It is argued that in a cloud of optical thickness τ_C the fraction P_{ref} of all reflected photons that penetrate to a maximum depth between τ and $\tau + \Delta\tau$ is represented by,

$$P_{ref}(\tau) = \frac{R(\tau + \Delta\tau) - R(\tau)}{R(\tau_C)}. \quad (2)$$

Here $R(\tau)$ is the reflectance from the portion of the cloud above the level $\tau=\tau(z)$ (i.e., calculated for a cloud layer between cloud top and $\tau(z)$ with lower layers absent). Normalizing with $\Delta\tau$ the vertical weighting function $w(\tau)$ gets,

$$w(\tau) = \frac{R(\tau + \Delta\tau) - R(\tau)}{R(\tau_C)} \cdot \frac{1}{\Delta\tau}. \quad (3)$$

To obtain a VWF $W(z)$ in units of [% m^{-1}] referring to the geometrical thickness of the cloud, we converted $w(z)$ considering that $\Delta\tau=b_{ext}(z)\cdot\Delta z$. By multiplying $w(z)$ with the vertical profile of the extinction coefficient $b_{ext}(z)$ it is,

$$W(z) = w(z) \cdot b_{ext}(z) \cdot 100\,\%. \quad (4)$$

Thus $W(z)$ gives the percentage contribution of each cloud layer to the radiance observed above cloud top.

The vertical profile of the cloud top reflectance R used to calculate $W(z)$ is obtained from radiative transfer simulations similar to the simulations presented in Sect. 4. The input for the cloud layer is identical to Case A matching the observed R at VIS wavelengths. According to the method described by Platnick (2000) the surface reflectance was set to zero. Thus no multiple reflections between the surface and the cloud layer

ACPD
9, 13801–13842, 2009

occur in the simulations which ensures that $W(z)$ is normalized between cloud base z_{base} and cloud top z_{top} by,

$$\int_{z_{base}}^{z_{top}} W(z)\,dz = 1. \quad (5)$$

As discussed by Platnick (2000) for a low surface albedo (measurements during ASTAR have shown values below 0.05) this assumption has no significant impact on $W(z)$. With the same argumentation, aerosol which also scatters/reflects radiation below the cloud base was excluded from the simulations.

The calculated $W(z)$ for the two exemplary wavelengths (1510 nm and 1710 nm) are given in Fig. 8a. In Fig. 8b $W(z)$ is accumulated over the altitude starting with 0 % at cloud top. For both wavelengths the weighting shows the highest contribution for cloud layers close to the cloud top at 1700 m altitude. The maximum values of $W(z)$ are found to be higher for λ=1510 nm than for λ=1710 nm. With the higher values of $W(z)$ the cloud top reflectance at λ=1510 nm is dominated stronger by absorption by particles at cloud top than R at λ=1710 nm. Therefore, R at λ=1510 nm is more suitable to retrieve the particle size at cloud top.

A decrease of $W(z)$ with increasing cloud depth is observed for both wavelengths. The accumulated weighting (Fig. 8b) shows that 50 % of the measured signal at 1710 nm wavelength is related to the cloud layer above 1410 m. Only 10% correspond to the cloud layer below 1060 m. For λ=1510 nm a steeper slope is obtained (50 % at 1440 m).

In this way a characteristic photon penetration depth z_{50} is determined for all wavelengths. It specifies the depth of the cloud layer (measured from cloud top) which is related to 50 % of the measured reflectance signal. z_{50} is shown in Fig. 7 for the wavelength range 1300–1800 nm. The spectral differences of z_{50} are mostly due to absorption of radiation within the cloud. At wavelengths dominated by water vapor absorption (λ=1350–1500) the minimum of z_{50} with values below 150 m is obtained. Between 1500 nm (high ice absorption) and 1700 nm (low ice absorption) z_{50} increases

ACPD
9, 13801–13842, 2009

from about 160 m to 195 m. This amplifies the assumption that the observed absorption signal in the radiance measurements for λ=1490 nm is related to layers close to the cloud top while the absorption observed at longer wavelengths about 1710 nm includes particles located at lower cloud layers.

These spectral differences in the VWF provide a tool to retrieve information on the vertical distribution of the cloud particle effective diameter, as described by Chen et al. (2007). In contrast to Chen et al. (2007) the investigations shown here are limited to a small wavelength range (1400–1800 nm). However, this range includes one spectral maximum and one spectral minimum of ice and liquid water absorption and is covered by the SMART-Albedometer measurements with sufficient spectral resolution to analyze these spectral differences. Wavelengths where liquid water and ice absorption are strong can be used to derive the particle properties at cloud top, whereas wavelengths with weaker absorption give information on particles located at lower cloud layers. Utilizing the spectral differences between the maxima of ice and liquid water absorption, separate vertical profiles for ice crystals and liquid water droplets can be derived.

The SMART-Albedometer measurements of R presented in Fig. 4a showed that for wavelengths below λ=1700 nm stronger absorption is measured than shown by the simulations. The maximum differences overlap with the ice absorption maximum (λ=1490 nm). At wavelengths between 1700–1800 nm weaker absorption is observed. Following the findings discussed above the strong absorption for λ=1490 nm implies that large ice crystals are present in the uppermost cloud layers. On the other hand, the high values of R between 1700–1800 nm wavelength indicate small cloud particles at cloud top and at lower cloud layers. This conclusion differs from the vertical distribution of ice crystals and liquid water droplets obtained by the in situ measurements. This may explain the discrepancy between simulated and measured cloud top reflectance.

ACPD
9, 13801–13842, 2009

6 Ice crystals at cloud top

The analysis of the VWF calculated for the radiance measurements suggests that ice crystals might be present at cloud top of the ABM clouds observed on 7 April. Therefore, the original cloud simulated with Case A was modified in Case C and D (Fig. 3) by adding a thin ice layer at cloud top. For Case C the ice layer is situated within the original cloud (mixed-phase cloud top); for Case D an ice layer is added above the cloud top as illustrated in Fig. 3. The optical thickness of the thin ice layer was set to 0.5 with ice crystal effective diameter similar to the ice layer at cloud base ($D^{\mathrm{I}}_{\mathrm{eff}}$=103 μm, column shape). Due to adding the ice layer, the total optical thickness of the cloud is adjusted to τ=15.0 for Case C and τ=14.5 for Case D.

The spectral cloud top reflectance R simulated for the two cases C and D is shown in Fig. 8. For both cases almost identical results are obtained. Compared to the simulations presented above (Case A and B), these simulations fit for all wavelengths into the uncertainty range of the observed R. Especially the spectral pattern in the wavelength range dominated by ice and liquid water absorption is closer to the measurements as simulated without the additional ice layer. This reveals that ice crystals situated at cloud top are necessary to explain the observed absorption features with strong absorption at 1490 nm and weak absorption at wavelengths about 1750 nm.

From the in situ measurements of microphysical cloud properties no solid evidence of ice crystals in the uppermost cloud layer was found. Above 1500 m altitude only 7 out of 69 measurements of the Polar Nephelometer indicated ice crystals with asymmetry parameters below 0.82 (cf. Fig. 1). These measurements do not significantly alter the volumetric asymmetry parameter ($\langle g \rangle$=0.85) calculated for this cloud layer. The CPI registered ice particles only at five times. The measured low ice concentration is probably caused by the low sampling time in this cloud layer which is limited due to performing ascents and descents into the cloud instead of horizontal legs at a fixed altitude. With the slightly varying cloud top height the ice crystals might not be represented well in the measurements. Furthermore the horizontal variability of the ABM

ACPD
9, 13801–13842, 2009

clouds as shown by Gayet et al. (2009) and the time delay between in situ and remote sensing measurements may explain the different results of both methods.

7 Simulation of backscatter glory

The backscatter glory is an optical phenomenon based on single scattering processes and typical for spherical liquid water droplets. The intensity variations of the reflected radiation reflect the single scattering phase function of the liquid water droplets located at cloud top. Therefore, the observations of backscatter glories are used by e.g. Gedzelman (2003); Mayer et al. (2004) to retrieve the cloud droplet effective diameter.

During the measurement flights of ASTAR 2007 frequently backscatter glories have been observed by eye and photo camera. The photographs have not been taken systematically. However, two exemplary photographs taken on 7 April 11:05 UTC (78° N, 11.5° E) and 10 April 11:31 UTC are shown in Fig. 9. The ice indices measured above these clouds are slightly lower than for the ABM cloud for which the closure study is conducted. However, the values are higher than expected for pure liquid water clouds and indicate the presence of ice crystals at the same time the glories have been observed.

The presence of ice crystals at the cloud top of the observed ABM clouds was also concluded in Sect. 6. However, the observations of the backscatter glory puts this finding into question as the scattering phase function $\mathcal{P}(\vartheta)$ of ice crystals does not exhibit this feature. Figure 10 shows an extract of $\mathcal{P}(\vartheta)$ of the ice crystals (columns) and liquid water droplet populations used in the simulations analyzed above. Displayed are the three wavelengths λ=450 nm, λ=550 nm and λ=600 nm representative for the blue, green and red color of the visible solar radiation.

For ice crystals $\mathcal{P}(\vartheta)$ increases with increasing scattering angle in the range of scattering angles considered (Fig. 10a). This is related to the large particle size of $D_{\mathrm{eff}}^{\mathrm{I}}$=103 μm. The larger the particle size, the higher the backscattering (ϑ=180°) which

is mainly caused by specular reflection at the ice crystal surface. In addition to the maximum at ϑ=180° liquid water droplets (Fig. 10b) have a slight secondary maximum of $\mathcal{P}(\vartheta)$ at about ϑ=178° for 550 nm and 600 nm wavelengths and at about ϑ=178.5° for 450 nm. This second maximum causes the increased intensity of reflected radiation observed on the glory phenomena. The shift of the maximum for the different wavelengths produces the rainbow-like colors of the glories.

3-D Monte Carlo simulations have been performed to simulate the backscatter glory. Applying the methods presented by Mayer and Emde (2007) the angular distribution of radiation scattered into the backscatter range $\vartheta \geq 175°$ was calculated. Considering the solar zenith angle of 71° this corresponds to viewing zenith angles between 71° and 76°. For the 3-D radiative transfer simulations the MYSTIC code (Monte Carlo code for the physically correct tracing of photons in cloudy atmospheres) embedded in the *libRadtran* package was applied (Mayer, 1999, 2000, 2009). With MYSTIC the backscattered radiance was calculated for the flight altitude of 1800 m approximately 200 m above cloud top. In the simulations the extension of the solar disk of 0.5° is considered. Therefore, the radiance distribution is convoluted with $\sqrt{\theta_S^2 - (\theta - \theta_0)^2}$ where θ_0 is the solar zenith angle specified for the center of the solar disk and θ_S the angular radius of the solar disk. The convolution causes a slight smoothing of the resulting radiance distribution which is not essential for the conclusions presented here but large enough to be considered.

Finally, the radiances were converted to color (R, G, B) values following the procedure by the Commission Internationale de l'Éclairage (CIE, CIE, 1986). The procedure is implemented in the C program *specrend.c* provided by CIE which was applied here http://www.fourmilab.ch/documents/specrend/.

The angular distribution of the R, G, B colors were calculated for the three clouds Case A, C and D. Values of R, G, B normalized to the value at backscattering angle ϑ=180° are shown in the left panels of Fig. 11 for a viewing azimuth angle parallel to the azimuth of the Sun. In the right panels R, G, B images are calculated by rotating the angular distributions shown in the left panels. The rotating of the simulations

for one single viewing azimuth is justified as additional simulations showed that the glory is symmetrical to the backscattering angle. In the results simulated for the ABM cloud dominated by liquid water at cloud top (Case A) the backscatter glory is visible. Although the simulations exhibit some noise, the normalized radiance reflects the scattering phase function of the liquid water droplets (cf. Fig. 10). The noise is due to the number of photons used in the Monte Carlo radiative transfer simulations but is not essential for the conclusions presented here. The wavelength shift of the secondary maximum is only weak in the simulations which results in the almost white color of the rotated image. This is due to the broad number size distribution of the liquid water droplets at cloud top used in the simulations. As shown by Mayer and Emde (2007) the colors of the backscatter glory are less pronounced if broad droplet size distributions are used. These findings are contrary to the glory photographs presented in Fig. 9 but may result from the differences of the location of the in situ measurements and the location the photographs were taken.

For Case C where an ice layer of τ=0.5 is situated inside the uppermost cloud layer the backscatter glory is weaker than observed for Case A, but still visible in the rotated R, G, B image. Close to the backscattering angle the radiance is higher than in Case A. This spot is caused by the enhanced backscattering of the ice crystals. In airborne observations this spot is covered by the shadow of the aircraft and hence not visible. These results show that ice crystals of an optical thickness less than 0.5 situated inside the liquid water layer (mixed-phase cloud top, Case C) can reproduce the simultaneous observation of ice absorption and glory phenomena. Contrarily, Case D where the same ice layer is located above the liquid water layer the backscatter glory was not reproduced by the simulations. The angular distribution of the radiance shows similar characteristics as the scattering phase function of the ice crystals (cf. Fig. 10). From this analysis it is concluded that Case D does not suit the remote sensing observation above ABM clouds obtained during ASTAR 2007.

ACPD
9, 13801–13842, 2009

8 Conclusions

Airborne measurements of cloud top reflectance R obtained during the ASTAR 2007 campaign have been analyzed to retrieve information on the vertical distribution of ice crystals in ABM clouds. For this purpose, spectral radiative transfer simulations of R are performed and compared to the measured R. The radiative transfer simulations based on the microphysical properties obtained during ASTAR 2007 (Case A0) underestimate R over the entire wavelength range covered by the SMART-Albedometer by a factor of 1.5. This indicates that the cloud optical thickness is underestimated by the in situ measurements probably caused by cloud inhomogeneities which bias the averaged cloud microphysical properties. Scaling the cloud optical thickness (Case A) the radiative transfer simulations failed to reproduce the spectral pattern of R observed in the wavelength range dominated by ice and liquid water absorption (1500–1800 nm). Varying the ice optical fraction (Case B1–B6) did not improve the results significantly.

Agreement within the measurement uncertainties between measurements and simulations was obtained when a thin ice layer of τ=0.5 was added in the simulations at cloud top (Cases C and D). This suggests that ice crystals were present in the uppermost layers of the observed ABM clouds. Analysis of the in situ measurements could neither confirm nor reject these results. In general these data showed a cloud top dominated by liquid water droplets whereas ice crystals are dominant at lower cloud levels similar to the observation by Gayet et al. (2009). The absence of ice crystals in the in situ measurements at cloud top is probably due to the flight strategy (vertical profiling) providing only short passages of this cloud layer and the horizontal variability of ABM clouds as shown by Gayet et al. (2009).

On top of the investigated clouds backscatter glories have been observed which generally indicate the presence of liquid water droplets at cloud top. This observation was validated by 3-D radiative transfer simulations focusing on the radiation within the backscatter region. Implementing ice crystals directly within the uppermost cloud layer (Case C) reproduced a weak but visible backscatter glory and explains the ob-

ACPD
9, 13801–13842, 2009

servations. Situating the thin ice layer above the original cloud (Case D) eliminated the backscatter glory.

These findings implicate that the presence of ice crystals at cloud top may alter the radiative properties of ABM clouds compared to homogeneous mixed clouds. The solar radiative cooling by ABM clouds (e.g., Schweiger and Key, 1994; Dong and Mace, 2003; Ehrlich, 2009) might be stronger than calculated due to the enhanced side scattering of ice crystals. The enhanced ice absorption by these ice crystals will also bias the ice indices utilized to identify the cloud thermodynamic phase (Acarreta et al., 2004; Ehrlich et al., 2008a). Compared to a cloud top layer dominated by liquid water a mixed-phase cloud top layer of ABM clouds bias the ice indices towards higher values.

Furthermore, the evidence for the existence of ice crystals at the top of ABM clouds has implications for the physical processes occurring within these clouds. The common vertical structure of ABM clouds with a liquid water layer at cloud top and an ice layer with precipitating ice crystals below as described by e.g., McFarquhar et al. (2007); Shupe et al. (2006) might not generally be valid. Ice crystals are present within the entire cloud although liquid water droplets are dominant at cloud top. These findings suggest conclusions on the dominating physical ice production mechanisms. Durant and Shaw (2005) describe the ice nucleation mechanism due to evaporation freezing which occurs mainly at the cloud top and in downdrafts where liquid water droplets evaporate. This process was analyzed by Fridlind et al. (2007) and Fan et al. (2008) for ABM clouds. The observed clouds were well reproduced by dynamical models if the enhanced ice nucleation by droplet evaporation freezing was considered. The location of the maximum ice nucleation rate is found near the cloud top and cloud base which is in agreement with the findings of this study. Contrarily, simulations neglecting evaporation freezing show ice crystals to be dominant at lower cloud layers only (e.g., Harrington et al., 1999; Morrison et al., 2008; Avramov and Harrington, 2008).

The analysis of the spectral cloud top reflectance measured by the SMART-Albedometer has shown that the spectral information within the wavelength range 1500–1800 nm is essential to retrieve information on the ice crystal properties. In this

regard the VWF of the SMART-Albedometer measurements was investigated. Using the methods described by Platnick (2000) the contribution of each cloud layer to the ice and liquid water absorption reflected in the measurements of R was quantified by the VWF $W(z)$. The vertical profile of $W(z)$ showed that the signal measured by the SMART-Albedometer is dominated by absorption processes within the uppermost cloud layers of less than 200 m thickness which is in agreement with the findings presented by Platnick (2000). However, $W(z)$ calculated for different wavelengths revealed spectral differences of the vertical weighting of the SMART-Albedometer measurements. These differences result from the spectral pattern of the ice and liquid water absorption. Consequently, by analyzing the spectral pattern of the measured R information on the vertical distribution of cloud particles can be retrieved.

Similar investigations have been conducted by e.g., Chang and Li (2002, 2003) and Chen et al. (2008) who used four different wavelength bands of MODIS measurements (1250 nm, 1650 nm, 2150 nm and 3750 nm) to retrieve the vertical variation of the cloud droplet effective diameter from remote sensing. The investigations presented in this study suggest that these methods are adaptive to high spectral measurement of a small wavelength region as obtained by the SMART-Albedometer. The only requirement is that the measurements resolve changes in the spectral absorption of ice and liquid water.

Acknowledgements. This research was funded by the German Research Foundation (DFG, WE 1900/8-1) and AWI. The Leibniz-Institute for Tropospheric Research, Leipzig, Germany is acknowledged for funding the integration of the SMART-Albedometer on the Polar 2 aircraft. We thank Ping Yang, Department of Atmospheric Sciences at Texas A&M University, for providing the library of optical properties of ice crystals used in our simulations. For the technical support during the ASTAR campaign we want to acknowledge the companies *enviscope* GmbH and OPTIMARE GmbH. Thomas Wagner and Steffen Beirle, both Max Planck Institute for Chemistry, Mainz, Germany, are thanked for the useful discussion that improved the quality of this paper.

References

Acarreta, J. R., Stammes, P., and Knap, W. H.: First retrieval of cloud phase from SCIAMACHY spectra around 1.6 μm, Atmos. Res., 72, 89–105, doi:10.1016/j.atmosres.2004.03.027, 2004. 13822

Avramov, A. and Harrington, J. Y.: The influence of ice crystal habit on simulations of Arctic mixed-phase clouds, in: Proc. of the ICCP Conference, Cancun, Mexico, 7–11 July 2008. 13822

Bierwirth, E., Wendisch, M., Ehrlich, A., Heese, B., Tesche, M., Althausen, D., Schladitz, A., Müller, D., Otto, S., Trautmann, T., Dinter, T., von Hoyningen-Huene, W., and Kahn, R.: Spectral surface albedo over Morocco and its impact on the radiative forcing of Saharan dust, Tellus, 61B, 252–269, 2009. 13806

Boudala, F. S., Isaac, G. A., Cober, S. G., and Fu, Q.: Liquid fraction in stratiform mixed-phase clouds from in situ observations, Q. J. Roy. Meteor. Soc., 130, 2.919–2.931, doi: 10.1256/qj.03.153, 2004. 13803, 13805

Chang, F. L. and Li, Z. Q.: Estimating the vertical variation of cloud droplet effective radius using multispectral near-infrared satellite measurements, J. Geophys. Res., 107, 4257, 2002. 13806, 13823

Chang, F. L. and Li, Z. Q.: Retrieving vertical profiles of water-cloud droplet effective radius: Algorithm modification and preliminary application, J. Geophys. Res., 108, 4763, 2003. 13806, 13823

Chen, R. Y., Chang, F. L., Li, Z. Q., Ferraro, R., and Weng, F. Z.: Impact of the vertical variation of cloud droplet size on the estimation of cloud liquid water path and rain detection, J. Atmos. Sci., 64, 3843–3853, 2007. 13816

Chen, R. Y., Wood, R., Li, Z. Q., Ferraro, R., and Chang, F. L.: Studying the vertical variation of cloud droplet effective radius using ship and space-borne remote sensing data, J. Geophys. Res., 113, D00A02, 2008. 13806, 13823

CIE: Standard on colorimetric observers, Commission Internationale de lEclairage (CIE) cie s002 edition, 1986. 13819

Cober, S. G., Isaac, G. A., Korolev, A. V., and Strapp, J. W.: Assessing cloud-phase conditions, J. Appl. Meteorol., 40, 1967–1983, 2001. 13803, 13805

Curry, J. A., Rossow, W. B., Randall, D., and Schramm, J. L.: Overview of Arctic cloud and radiation characteristics, J. Climate, 9, 1731–1764, 1996. 13804

Dong, X. Q. and Mace, G. G.: Arctic stratus cloud properties and radiative forcing derived from ground-based data collected at Barrow, Alaska, J. Climate, 16, 445–461, 2003. 13822
Durant, A. J. and Shaw, R. A.: Evaporation freezing by contact nucleation inside-out, Geophys. Res. Lett., 32, L20814, doi:10.1029/2005GL024175, 2005. 13822
Ehrlich, A.: The Impact of Ice Crystals on Radiative Forcing and Remote Sensing of Arctic Boundary-Layer Mixed-Phase Clouds, Ph.D. thesis, Johannes Gutenberg University Mainz, Germany, 2009. 13810, 13822
Ehrlich, A., Bierwirth, E., Wendisch, M., Gayet, J.-F., Mioche, G., Lampert, A., and Heintzenberg, J.: Cloud phase identification of Arctic boundary-layer clouds from airborne spectral reflection measurements: Test of three approaches, Atmos. Chem. Phys., 8, 7493–7505, 2008a, http://www.atmos-chem-phys.net/8/7493/2008/. 13806, 13807, 13808, 13809, 13810, 13812, 13822, 13832, 13840
Ehrlich, A., Wendisch, M., Bierwirth, E., Herber, A., and Schwarzenböck, A.: Ice crystal shape effects on solar radiative properties of Arctic mixed-phase clouds – Dependence on microphysical properties, Atmos. Res., 88, 266–276, 2008b. 13804
Fan, J., Ovtchinnikov, M., Comstock, J., McFarlane, S., and Khain, A.: Modeling Arctic mixed-phase clouds and associated ice formation, in: Proc. of the ICCP Conference, Cancun, Mexico, 7–11 July 2008. 13804
Gayet, J. F., Mioche, G., Dörnbrack, A., Ehrlich, A., Lampert, A., and Wendisch, M.: Microphysical and optical properties of Arctic mixed-phase clouds – The 9 April 2007 case study, Atmos. Chem. Phys. Discuss., 9, 11333–11366, 2009, http://www.atmos-chem-phys-discuss.net/9/11333/2009/. 13805, 13806, 13807, 13808, 13818, 13821
Gedzelman, S. D.: Simulating glories and cloudbows in color, Appl. Optics, 42, 429–435, 2003. 13818
Harrington, J. Y., Reisin, T., Cotton, W. R., and Kreidenweis, S. M.: Cloud resolving simulations of Arctic stratus – Part II: Transition-season clouds, Atmos. Res., 51, 45–75, 1999. 13804, 13805, 13822
Korolev, A. V., Isaac, G. A., Cober, S. G., Strapp, J. W., and Hallett, J.: Microphysical characterization of mixed-phase clouds, Q. J. Roy. Meteor. Soc., 129, 39–65, 2003. 13803, 13805
Lampert, A., Ehrlich, A., Dörnbrack, A., Jourdan, O., Gayet, J.-F., Mioche, G., Shcherbakov, V., Ritter, C., and Wendisch, M.: Microphysical and radiative characterization of a subvisible midlevel Arctic ice cloud by airborne observations – a case study, Atmos. Chem. Phys., 9,

2647–2661, 2009, http://www.atmos-chem-phys.net/9/2647/2009/. 13806
Lawson, R. P., Baker, B. A., Schmitt, C. G., and Jensen, T. L.: An overview of microphysical properties of Arctic clouds observed in May and July 1998 during FIRE ACE, J. Geophys. Res., 106, 14989–15014, 2001. 13805
Mayer, B.: I3RC phase 1 results from the MYSTIC Monte Carlo model, in: Intercomparison of three-dimensional radiation codes: Abstracts of the first and second international workshops, 49–54, University of Arizona Press, 1999. 13819
Mayer, B.: I3RC phase 2 results from the MYSTIC Monte Carlo model, in: Intercomparison of three-dimensional radiation codes: Abstracts of the first and second international workshops, 107–108, University of Arizona Press, 2000. 13819
Mayer, B.: Radiative transfer in the cloudy atmosphere, The European Physical Journal Conferences, 1, 75–99, 2009. 13819
Mayer, B. and Emde, C.: Comment on "Glory phenomenon informs of presence and phase state of liquid water in cold clouds" by Anatoly N. Nevzorov, Atmos. Res., 84, 410–419, 2007. 13819, 13820
Mayer, B. and Kylling, A.: Technical note: The libRadtran software package for radiative transfer calculations – description and examples of use, Atmos. Chem. Phys., 5, 1855–1877, 2005, http://www.atmos-chem-phys.net/5/1855/2005/. 13809
Mayer, B., Schröder, M., Preusker, R., and Schüller, L.: Remote sensing of water cloud droplet size distributions using the backscatter glory: A case study, Atmos. Chem. Phys., 4, 1255–1263, 2004, http://www.atmos-chem-phys.net/4/1255/2004/. 13818
McFarquhar, G. M. and Cober, S. G.: Single-scattering properties of mixed-phase Arctic clouds at solar wavelengths: Impacts on radiative transfer, J. Climate, 17, 3799–3813, 2004. 13803
McFarquhar, G. M., Zhang, G., Poellot, M. R., Kok, G. L., Mccoy, R., Tooman, T., Fridlind, A., and Heymsfield, A. J.: Ice properties of single-layer stratocumulus during the Mixed-Phase Arctic Cloud Experiment: 1. Observations, J. Geophys. Res., 112, D24201, doi:10.1029/2007JD008633, 2007. 13804, 13805, 13822
Miles, N. L., Verlinde, J., and Clothiaux, E. E.: Cloud droplet size distributions in low-level stratiform clouds, J. Atmos. Sci., 57, 295–311, 2000.
Morrison, H., Curry, J., and Khvorostyanov, V.: A new double-moment microphysics parameterization for application in cloud and climate models. Part II: Single-column modeling of Arctic clouds, J. Atmos. Sci., 62, 1678–1693, 2005. 13804
Morrison, H., Pinto, J. O., Curry, J. A., and McFarquhar, G. M.: Sensitivity of modeled Arctic

mixed-phase stratocumulus to cloud condensation and ice nuclei over regionally varying surface conditions, J. Geophys. Res., 113, D05203, doi:10.1029/2007JD008729, 2008. 13804, 13822

Pinto, J. O.: Autumnal mixed-phase cloudy boundary layers in the Arctic, J. Atmos. Sci., 55, 2016–2038, 1998. 13804

Platnick, S.: Vertical photon transport in cloud remote sensing problems, J. Geophys. Res., 105, 22919–22935, 2000. 13805, 13814, 13815, 13823

Prenni, A. J., Harrington, J. Y., Tjernstrom, M., DeMott, P. J., Avramov, A., Long, C. N., Kreidenweis, S. M., Olsson, P. Q., and Verlinde, J.: Can ice-nucleating aerosols affect Arctic seasonal climate?, B. Am. Meteor. Soc., 88, 541, 2007. 13804

Schweiger, A. and Key, J.: Arctic ocean radiative fluxes and cloud forcing estimated from the ISCCP C2 cloud dataset, 1983–1990, J. Appl. Meteorol., 33, 948–963, 1994. 13822

Shupe, M. D. and Intrieri, J. M.: Cloud radiative forcing of the Arctic surface: The influence of cloud properties, surface albedo, and solar zenith angle, J. Climate, 17, 616–628, 2004. 13803, 13804

Shupe, M. D., Matrosov, S. Y., and Uttal, T.: Arctic mixed-phase cloud properties derived from surface-based sensors at SHEBA, J. Atmos. Sci., 63, 697–711, 2006. 13804, 13822

Shupe, M. D., Daniel, J. S., de Boer, G., Eloranta, E. W., Kollias, P., Long, C. N., Luke, E. P., Turner, D. D., and Verlinde, J.: A FOCUS ON MIXED-PHASE CLOUDS: The Status of Ground-Based Observational Methods, B. Am. Meteor. Soc., 89, 1549, 2008. 13803

Stamnes, K., Tsay, S., Wiscombe, W., and Jayaweera, K.: A numerically stable algorithm for discrete-ordinate-method radiative transfer in multiple scattering and emitting layered media, Appl. Optics, 27, 2502–2509, 1988. 13810

Turner, D. D., Ackerman, S. A., Baum, B. A., Revercomb, H. E., and Yang, P.: Cloud phase determination using ground-based AERI observations at SHEBA, J. Appl. Meteorol., 42, 701–715, 2003. 13803

Warren, S. G. and Brandt, R. E.: Optical constants of ice from the ultraviolet to the microwave: A revised compilation, J. Geophys. Res., 113, D14220, doi:10.1029/2007JD009744, 2008. 13833, 13835, 13836, 13838, 13839

Wendisch, M., Müller, D., Schell, D., and Heintzenberg, J.: An airborne spectral albedometer with active horizontal stabilization, J. Atmos. Oceanic Technol., 18, 1856–1866, 2001. 13806

Wendisch, M., Pilewskie, P., Pommier, J., Howard, S., Yang, P., Heymsfield, A. J., Schmitt, C. G., Baumgardner, D., and Mayer, B.: Impact of cirrus crystal shape on solar spec-

tral irradiance: A case study for subtropical cirrus, J. Geophys. Res., 110, D03202, doi:10.1029/2004JD005294, 2005.

Wieliczka, D. M., Weng, S. S., and Querry, M. R.: Wedge Shaped Cell For Highly Absorbent Liquids - Infrared Optical-Constants Of Water, Appl. Optics, 28, 1714–1719, 1989. 13833, 13835, 13836, 13838, 13839

Yang, P. and Liou, K. N.: Finite-difference time domain method for light scattering by small ice crystals in three-dimensional space, J. Opt. Soc. Am. A., 13, 2072–2085, 1996. 13810

Zuidema, P., Baker, B., Han, Y., Intrieri, J., Key, J., Lawson, P., Matrosov, S., Shupe, M., Stone, R., and Uttal, T.: An Arctic springtime mixed-phase cloudy boundary layer observed during SHEBA, J. Atmos. Sci., 62, 160–176, 2005.

ACPD

9, 13801–13842, 2009

Table 1. Microphysical and optical properties of the ABM cloud observed on 7 April 2007 (Case A0). For the closure study the cloud was divided into two sublayers, 800–1200 m and 1200–1600 m for which liquid water is situated in both layers. The adjusted values are used in the simulations of Case A where the cloud optical thickness was scaled to the observed cloud top reflectance.

			Measured Case A0	Scaled Case A
Liquid water	τ_W		7.5	16.9
800–1600 m	LWP	[g m^{-2}]	34.7	78.0
	D_{eff}^{W}	[μm]	14.8	14.8
Ice	τ_I		0.5	1.1
800–1200 m	IWP	[g m^{-2}]	17.2	38.7
	D_{eff}^{I}	[μm]	102.7	102.7
Total	τ		8.0	18.0
800–1600 m	TWP	[g m^{-2}]	51.9	116.7
	f_I^*		0.06	0.06
	f_I		0.33	0.33

ACPD
9, 13801–13842, 2009

Table 2. Microphysical and optical properties of ABM clouds Case B1–B6 characterized by different ice optical fractions f_l^*. The total cloud optical thickness is scaled to gain a cloud top reflectance similar to the observations for λ<1300 nm.

			B1	B2	B3	B4	B5	B6
Liquid Water	τ_W		18.0	16.2	14.0	9.6	6.0	0.0
800–1600 m	LWP	[g m^{-2}]	83.0	74.7	64.6	44.3	27.7	0.0
Ice	τ_l		0.0	1.8	3.5	6.4	9.0	9.0
800–1200 m	IWP	[g m^{-2}]	0.0	61.4	119.3	218.2	306.9	306.9
Total	τ		18.0	18.0	17.5	16.0	15.0	9.0
800–1600 m	TWP	[g m^{-2}]	83.0	136.1	183.9	262.5	334.6	306.9
	f_l^*		0.0	0.10	0.20	0.40	0.60	1.0
	f_l		0.0	0.45	0.65	0.83	0.92	1.0

ACPD
9, 13801–13842, 2009

Table 3. Spectral slope ice index I_S and principle component ice index I_P for the simulations of the clouds Case B1–B6. Additionally the values obtained from the SMART-Albedometer measurements are given.

	B1	B2	B3	B4	B5	B6	Measured
I_S	11.4	14.3	16.2	20.4	26.9	56.2	29.8
I_P	0.5	0.8	1.0	1.5	2.2	5.0	2.3

ACPD
9, 13801–13842, 2009

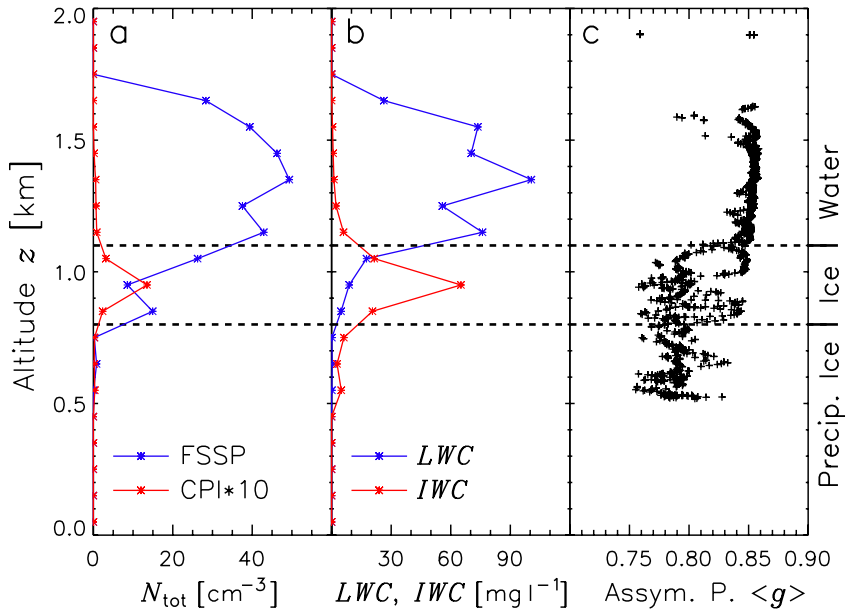

Fig. 1. Profiles of microphysical measurements obtained on 7 April 2007 (partly identical to Fig. 2 in Ehrlich et al., 2008a). Total particle number concentration N_{tot} measured by FSSP and CPI are given in panel (**a**); *LWC* and *IWC* in panel (**b**). The volumetric asymmetry parameter $\langle g \rangle$ obtained from the Polar Nephelometer is shown in panel (**c**).

ACPD
9, 13801–13842, 2009

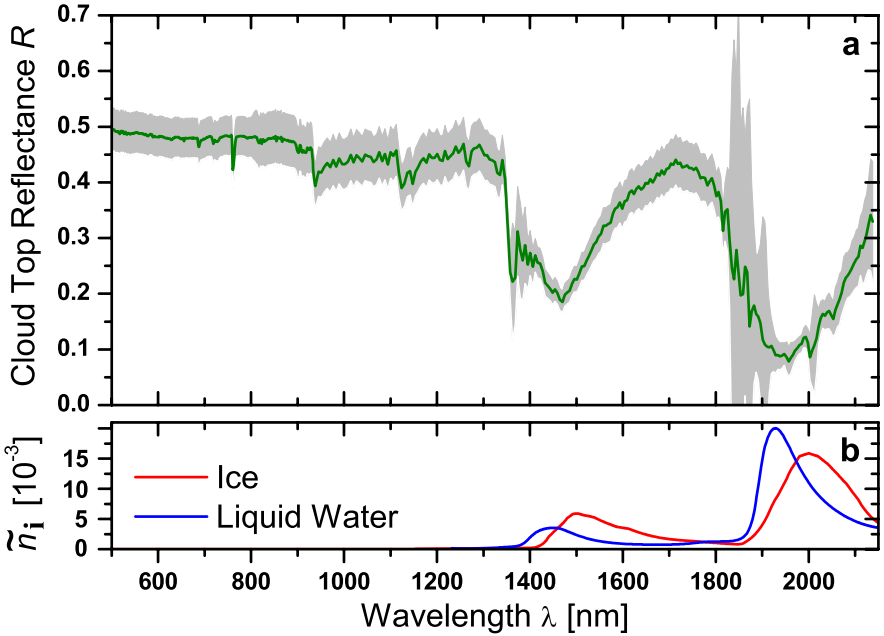

Fig. 2. Measured spectral cloud top reflectance R for ABM clouds observed on 7 April 2007. The measurement uncertainty is illustrated by the gray area. In panel (**b**) the refractive index $\tilde{n}_i$ of liquid water (Wieliczka et al., 1989) and ice (Warren and Brandt, 2008) is displayed.

ACPD
9, 13801–13842, 2009

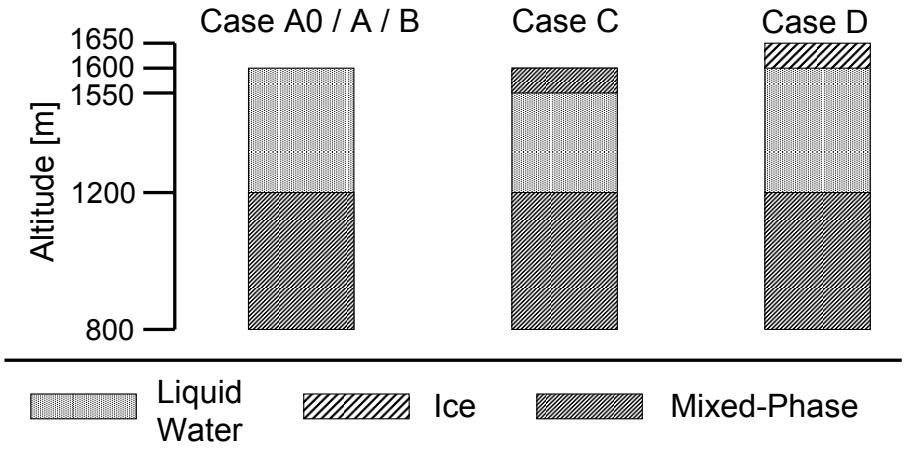

Fig. 3. Cloud geometries as represented in the radiative transfer simulations for the cases **(A)**, **(B)**, **(C)** and **(D)** and for the simulations using the measured cloud properties (Case A0).

ACPD
9, 13801–13842, 2009

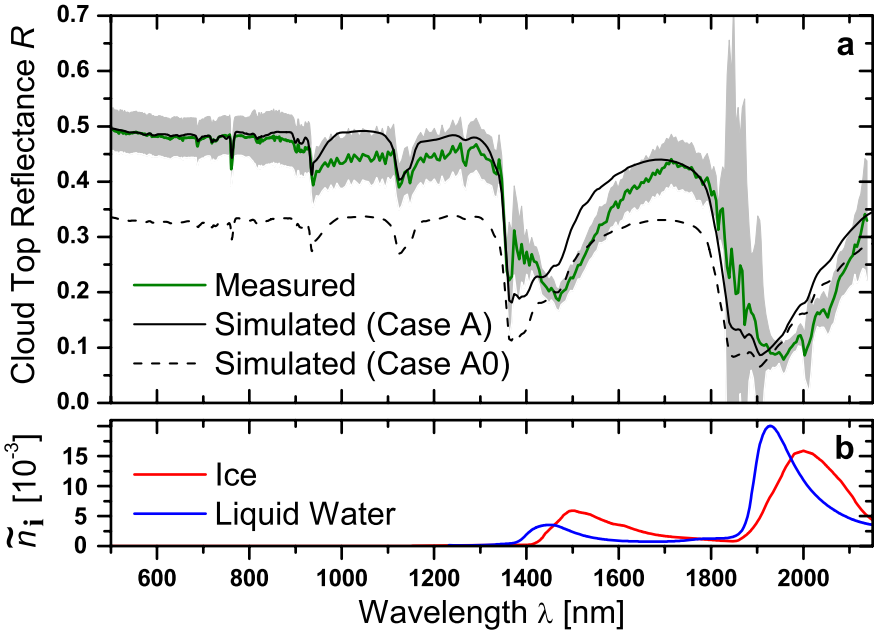

Fig. 4. Simulated (Cases A0 and A) and measured spectral cloud top reflectance R (panel **a**). The measurement uncertainty is illustrated by the gray area. In panel **(b)** the refractive index $\tilde{n}_i$ of liquid water (Wieliczka et al., 1989) and ice (Warren and Brandt, 2008) is displayed.

ACPD
9, 13801–13842, 2009

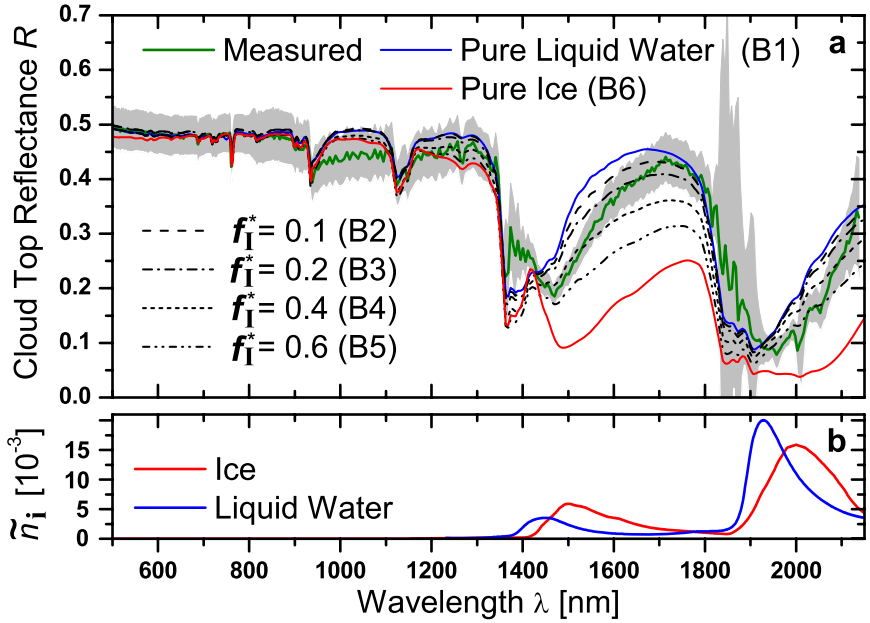

Fig. 5. Measured spectral cloud top reflectance R and simulated R for mixed-phase clouds of different f_l^* (Case B1–B6). The measurement uncertainty is illustrated by the gray area. In panel **(b)** the refractive index $\tilde{n}_i$ of liquid water (Wieliczka et al., 1989) and ice (Warren and Brandt, 2008) is displayed.

ACPD
9, 13801–13842, 2009

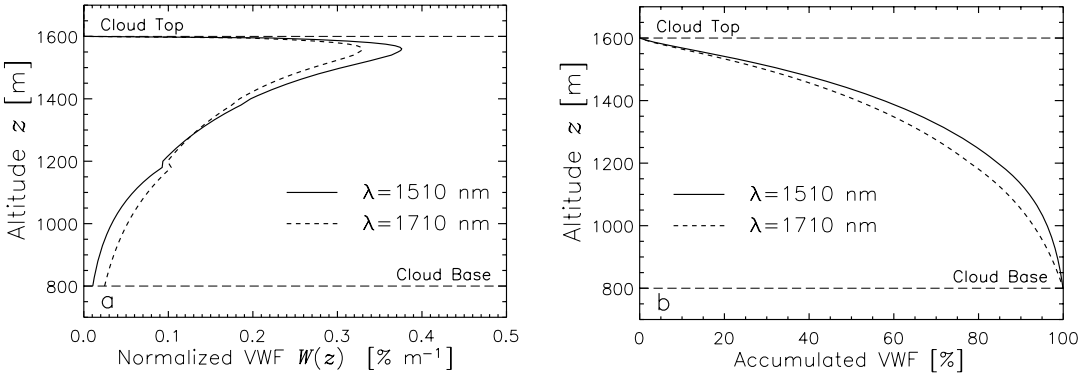

Fig. 6. Vertical weighting function $W(z)$ for the radiance measurements of the SMART-Albedometer with respect to absorption by the cloud particles using the cloud Case A (panel **a**). The accumulated weighting is given in panel **(b)**.

ACPD
9, 13801–13842, 2009

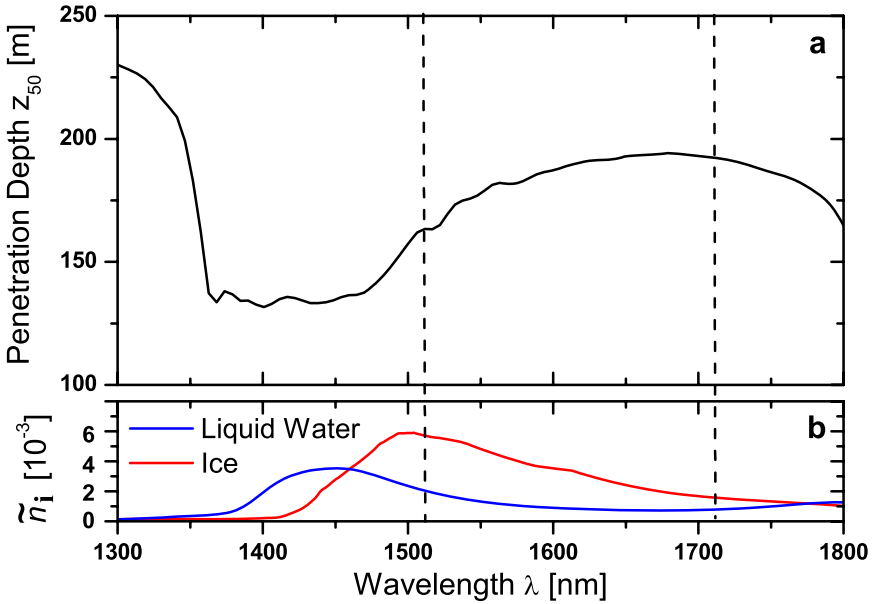

Fig. 7. Characteristic photon penetration depth characterizing the cloud top layer related to 50% of the measured signal (panel **a**). In panel **(b)** the refractive index $\tilde{n}_i$ of liquid water (Wieliczka et al., 1989) and ice (Warren and Brandt, 2008) is displayed.

ACPD
9, 13801–13842, 2009

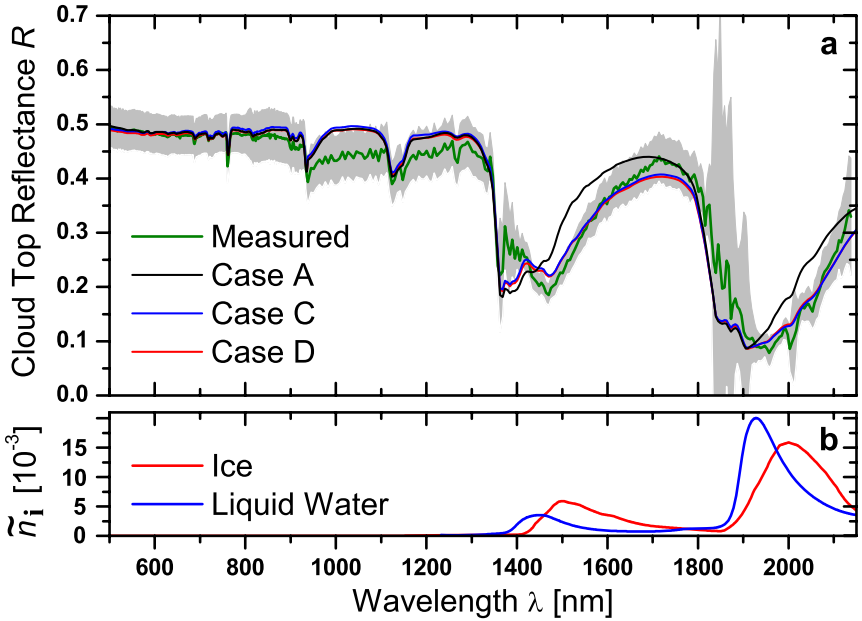

Fig. 8. Measured and simulated spectral cloud top reflectance R for cases A, C and D (panel **a**). The measurement uncertainty is illustrated by the gray area. In panel (**b**) the refractive index $\tilde{n}_i$ of liquid water (Wieliczka et al., 1989) and ice (Warren and Brandt, 2008) is displayed.

ACPD
9, 13801–13842, 2009

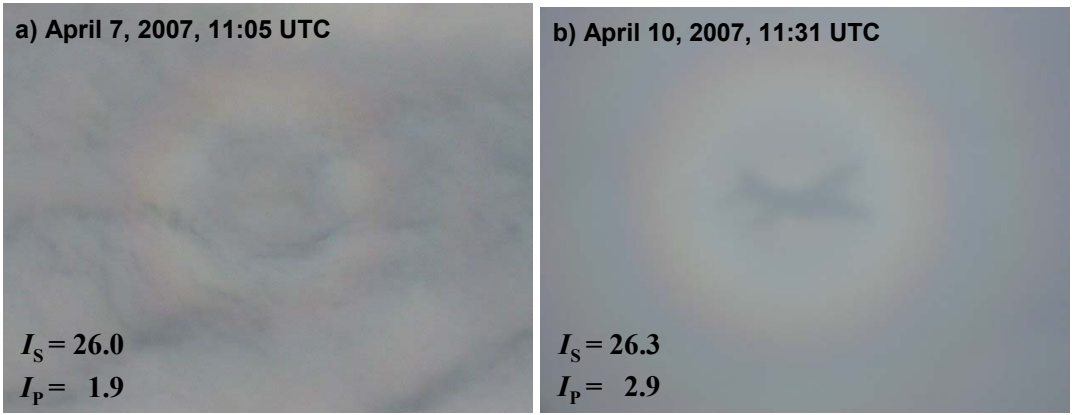

Fig. 9. Photographs of backscatter glories at cloud top. The left photograph was taken from the POLAR 2 aircraft on 7 April 11:05 UTC, the right on 10 April 11:31 UTC. The given ice indices I_S and I_P are derived from the SMART-albedometer measurements above these clouds (Ehrlich et al., 2008a).

ACPD
9, 13801–13842, 2009

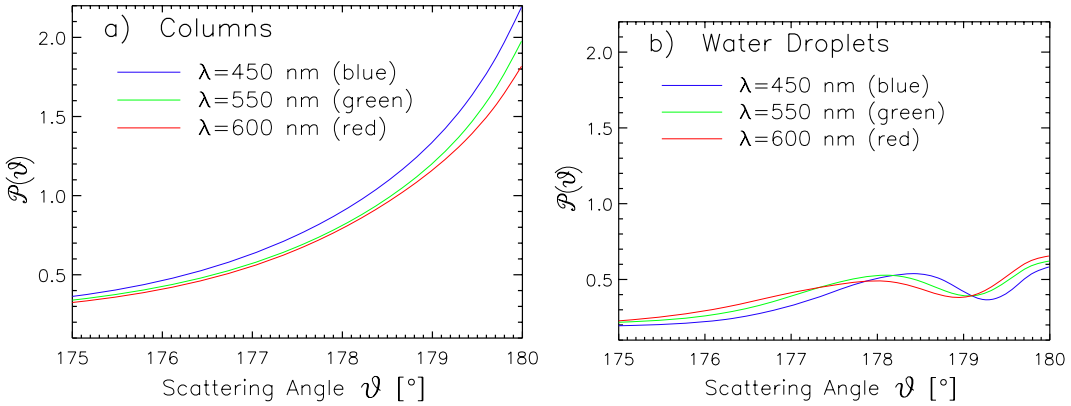

Fig. 10. Scattering phase function $\mathcal{P}(\vartheta)$ at three different wavelengths representative for the blue (450 nm), green (550 nm) and red (600 nm) color. The backscattering range between scattering angles ϑ=175–180° is shown. In panel (**a**) $\mathcal{P}(\vartheta)$ is given for the ice crystal population (columns), in panel b for the liquid water droplet population used in the simulations.

ACPD
9, 13801–13842, 2009

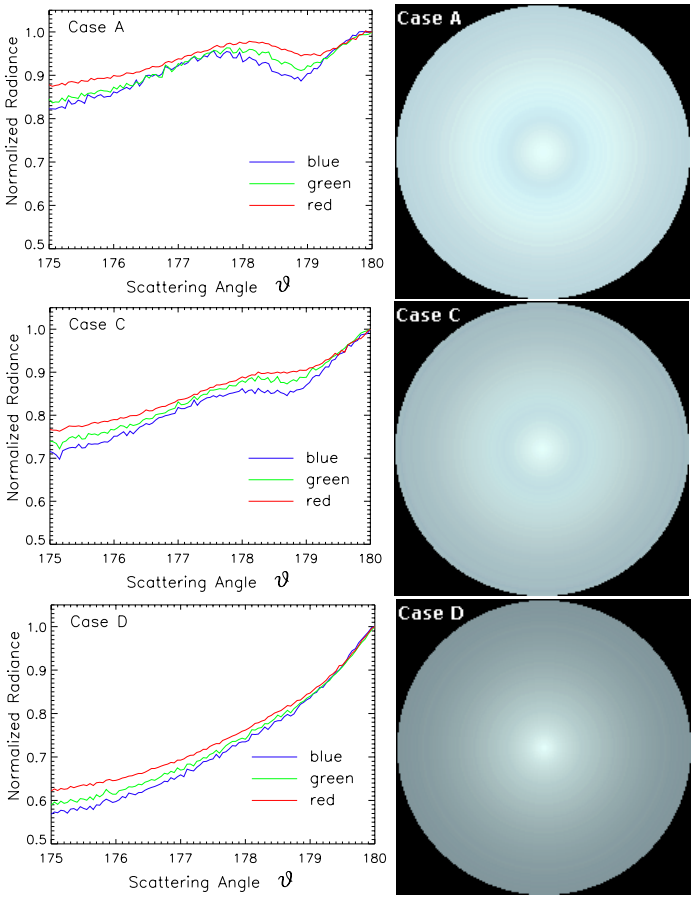

Fig. 11. Radiative transfer simulations of the angular distribution of spectral radiances of the backscattering region. Results are shown for the three cases **(A)**, **(C)** and **(D)**. The left panels show the angular distribution converted into R, G, B colors. The visualization of the glory is given in the right panels.

ACPD
9, 13801–13842, 2009